



Cite this: *Phys. Chem. Chem. Phys.*,
2022, 24, 10745

Relativistic nonorthogonal configuration interaction: application to $L_{2,3}$ -edge X-ray spectroscopy†

Adam Grofe  and Xiaosong Li *

In this article, we develop a relativistic exact-two-component nonorthogonal configuration interaction (X2C-NOCI) for computing L-edge X-ray spectra. This article to our knowledge is the first time NOCI has been used for relativistic wave functions. A set of molecular complexes, including SF_6 , $SiCl_4$ and $[FeCl_6]^{3-}$, are used to demonstrate the accuracy and computational scaling of the X2C-NOCI method. Our results suggest that X2C-NOCI is able to satisfactorily capture the main features of the $L_{2,3}$ -edge X-ray absorption spectra. Excitations from the core require a large amount of orbital relaxation to yield reasonable energies and X2C-NOCI allows us to treat orbital optimization explicitly. However, the cost of computing the nonorthogonal coupling is higher than in conventional CI. Here, we propose an improved integral screening using overlap-scaled density combined with a continuous measure of the generalized Slater–Condon rules that allows us to estimate if an element is zero before attempting a two-electron integral contraction.

Received 7th March 2022,
Accepted 12th April 2022

DOI: 10.1039/d2cp01127a

rsc.li/pccp

1 Introduction

In electronic structure theory, the power of a method is determined by the ability to simultaneously treat static correlation, dynamic correlation, orbital optimization, and relativistic effects in an efficient manner. Hartree–Fock (HF) theory efficiently treats orbital optimization but neglects both forms of correlation (under the definition of correlation by Löwdin).¹ Then multiconfigurational self-consistent field (MCSCF) combines both static correlation and orbital optimization. Finally, multireference configuration interaction (MRCI) and full CI incorporates orbital optimization and both forms of electron correlation, but are significantly more expensive than the other two methods. All of these methods use orthogonal orbitals and orthogonal configurations which through meticulous book keeping is able to represent all of the degrees of freedom exactly once (*i.e.*, no double counting). In orthogonal CI, the excitation operators are able to treat static correlation, dynamic correlation, and orbital optimization simultaneously (given a sufficient level of excitation). While these expansions are complete, they are inefficient in representing the wave function. The CI Hamiltonians are often sparse with many unimportant degrees of freedom. Thus, selected CI techniques seek to

compress the CI wave function by only including the most important degrees of freedom.^{2–5}

Nonorthogonal configuration interaction (NOCI) takes a different approach where the constraint on orthogonality of configurations is lifted.^{6–14} This allows the orbitals of each configuration to be optimized individually so that the configurations are at their lowest energy before mixing. This results in the NOCI Hamiltonian to become more dense compared to the conventional orthogonal CI but with the advantage of being able to recover static correlations with a smaller set of nonorthogonal determinants.¹¹ This makes NOCI particularly useful for studies of photochemical processes,^{15–23} where there exists a dense manifold of excited states. Additionally, several groups have developed post-NOCI methods to account of additional dynamic correlations.^{24–31}

In relativistic multi-configurational electronic structure methods, the scalar-relativistic effects are usually included variationally at the molecular orbital level. The spin–orbit coupling can be treated perturbatively^{32–35} or variationally,^{36–47} with the latter becoming more accurate for elements further down the periodic table. The inclusion of relativistic effects (scalar relativity and spin–orbit coupling) in NOCI is nontrivial, which, to the best of our knowledge, has never been developed. Relativistic orbital space is generally more dense due to their underlying spinor or bi-spinor electronic structure. As a result, obtaining optimized excited nonorthogonal determinants becomes more challenging. Recently, we proposed an effective algorithm to optimize excited determinants with desired electronic structure

Department of Chemistry, University of Washington, Seattle, Washington 98195, USA. E-mail: xsli@uw.edu

† Electronic supplementary information (ESI) available. See DOI: <https://doi.org/10.1039/d2cp01127a>

characteristics using the generalized block localized wave function (gBLW) method within the exact-two-component^{47–66} framework.^{67,68} With a carefully designed optimization space, the X2C-gBLW method is able to produce excited determinants including relativistic effects variationally. In this work, we extend the X2C-gBLW optimized nonorthogonal determinants to the NOCI regime. We introduce a set of integral screening approaches to reduce the computational cost of NOCI.

X-ray absorption spectroscopy is a good application of X2C-NOCI where excitations from the core introduce large perturbations to the electronic structure. Thus, explicit optimization of orbitals significantly lowers the energy of the determinant. Additionally, since both scalar relativity and spin-orbit couplings are significant in X-ray L-edge spectroscopy (excitations from the 2p core orbitals), variational treatment of relativistic effects are essential in accurate prediction of electronic excited states. There have been many advancements in modelling X-ray spectroscopy with orthogonal configuration interaction techniques that we will not review here, but will point the reader toward comprehensive reviews on the subject.^{69,70} In this article, we compute the L_{2,3}-edge spectra, which requires relatively large NOCI expansions in order to represent the whole spectrum.

2 Theoretical methods

Throughout this article we use the following notations to keep track of the nature of the index with respect to the basis.

- The Greek letters (μ , ν , λ , σ) index atomic spinor orbitals (AO's)
- Lowercase Latin letters (i , j , k) index occupied molecular orbitals (MO's)
- Uppercase Latin letters (I , J , K , L) index determinants
- Matrices in the sans Serif font **S** and **C** are in the atomic spinor basis
- Matrices in the bold font (**S** and **C**) are in the nonorthogonal molecular orbital basis
- Matrices in the blackboard font (\mathbb{S} and \mathbb{C}) are in the nonorthogonal determinant basis
- Quantities in the calligraphic font (\mathcal{E} and \mathcal{M}) are in the NOCI state basis

The X2C-NOCI wave function is expressed as a linear combination of nonorthogonal spinor configurations, which need to be obtained based on the chemical problem of interest. In this work, we use the X2C-gBLW^{67,68} approach to generate a set of nonorthogonal spinor configurations for X2C-NOCI. Because both the X2C transformation and gBLW approach are well established in the authors' previous work, brief reviews of the methods are presented in the Appendix.

2.1 Nonorthogonal configuration interaction

The X2C-gBLW procedure produces a series of determinants,⁶⁸ $|\psi_I\rangle$, each with a unique set of molecular orbitals that can be nonorthogonal between different configurations. A wave function expanded in nonorthogonal X2C configurations gives rise to the X2C-NOCI framework. The elements of CI Hamiltonian

can be computed using density matrices⁷¹ or corresponding orbitals,^{16,17,72–74} with the latter being more computational efficient.

To compute the corresponding orbitals, we begin by computing the overlap matrix of occupied molecular orbitals between any two determinants,

$$S_{IJ} = C_I^\dagger S C_J \quad (1)$$

where **S** is the spinor atomic orbital (AO) overlap matrix. **C**_{*I*} and **C**_{*J*} are the occupied orbital coefficient matrices for determinant *I* and *J*. It should be noted that the molecular orbitals within each determinant are orthonormal, but the orbitals between determinants may not be orthogonal to each other. Then performing a singular value decomposition of the overlap matrix in the nonorthogonal molecular orbital basis

$$S_{IJ} = \mathbf{U}_{IJ} \mathbf{s}_{IJ} \mathbf{V}_{IJ}^\dagger \quad (2)$$

yields the transformation matrices, **U**_{*IJ*} and **V**_{*IJ*}, and the diagonal matrix of singular values, **s**_{*IJ*}. The *k*-th singular value is the overlap between the *k*-th left and right corresponding orbitals. The corresponding orbitals are the set of orbitals that maximize the overlap between both sets of molecular orbitals. The corresponding orbitals can be computed using:

$$\tilde{\mathbf{C}}_I = \mathbf{C}_I \mathbf{U}_{IJ} \quad (3)$$

$$\tilde{\mathbf{C}}_J = \mathbf{C}_J \mathbf{U}_{IJ} \quad (4)$$

The overlap between two determinants in the NOCI determinant basis can be computed from the singular values and the left and right unitary matrices using

$$\mathbb{S}_{IJ} \equiv \det(S_{IJ}) = \det(\mathbf{U}_{IJ}) \det(\mathbf{V}_{IJ}) \det(\mathbf{s}_{IJ}) \quad (5)$$

where $\det(\mathbf{U}_{IJ})$ and $\det(\mathbf{V}_{IJ})$ are the determinants of the left and right unitary transformations, and yield the phase change induced within each determinant by the transformation to corresponding orbitals.⁷⁵ If the orbitals are real, $\det(\mathbf{U}_{IJ})$ and $\det(\mathbf{V}_{IJ})$ are either 1 or -1 , but for X2C these phases are complex valued where the modulus is 1.

The nonorthogonal one-electron transition density matrix⁷¹ in the AO basis can be defined as

$$\mathbf{D}_{IJ} = \tilde{\mathbf{C}}_I \mathbf{s}_{IJ}^{-1} \tilde{\mathbf{C}}_J^\dagger \quad (6)$$

which is used to compute the energy and properties. For NOCI, eqn (6) can be numerically unstable and zeroes in **s**_{*IJ*} must be detected to maintain numerical stability.¹⁶

The NOCI Hamiltonian in determinant basis, formulated in the AO-direct algorithm, can then be constructed using^{17,74}

$$\mathbb{H}_{IJ} = \mathbb{S}_{IJ} \left(\sum_{\mu\nu} \mathbf{D}_{IJ,\mu\nu} \mathbf{h}_{\mu\nu} + \frac{1}{2} \sum_{\mu\nu,\lambda\kappa} \mathbf{D}_{IJ,\mu\nu} \mathbf{D}_{IJ,\lambda\kappa} (\mu\nu||\lambda\kappa) \right) \quad (7)$$

where $\mathbf{h}_{\mu\nu}$ is the one-electron Hamiltonian matrix, and $(\mu\nu||\lambda\sigma)$ are the antisymmetrized two-electron integrals in Mulliken (chemical) notation. The one-electron Hamiltonian is the X2C Hamiltonian (see Appendix 1) that includes the scalar relativistic correction and one-electron spin-orbit coupling.

The two-electron spin-orbit terms have been approximated using the empirical scaling terms due to Boettger.⁷⁶

The NOCI coefficients can then be determined by solving the generalized eigenvalue problem

$$\mathbb{H}\mathbb{C}_n = \mathbb{S}\mathbb{C}_n\mathcal{E}_n \quad (8)$$

where \mathcal{E}_n and \mathbb{C}_n are the NOCI energy eigenvalues and eigenvectors. In the limit that the orbitals become orthogonal, the s_{IJ}^{-1} scaling of the transition density matrix elements in eqn (6) cancels with the determinant overlap \mathbb{S}_{IJ} in eqn (7) to yield the Slater–Condon rules.

2.2 Improved integral screening

The computational cost of eqn (7) formally scales as M^2N^4 , where M is the number of determinants and N is the number of basis functions. Usually M is much smaller than N in NOCI calculations, making the computation of the AO two-electron integrals and contraction the dominant cost. Kathir *et al.* reduced this cost through a reduced orbital basis set which decreased the number of integrals that need to be contracted.^{77,78} In an AO direct NOCI implementation, we choose to do the first contraction of the two-electron integrals with AO transition densities (*i.e.*, over indices λ, κ) by taking advantage of the integral and contraction screening developed for the AO Fock build,^{79,80}

$$\mathbf{G}_{IJ,\mu\nu}[\mathbf{D}_{IJ,\lambda\kappa}] = \sum_{\lambda\kappa} \mathbf{D}_{JI,\lambda\kappa}(\mu\nu|\lambda\kappa) \quad (9)$$

Then $\mathbf{D}_{IJ,\mu\nu}$ can be contracted with $\mathbf{G}_{IJ,\mu\nu}[\mathbf{D}_{JI,\lambda\kappa}]$ and multiplied by the overlap to yield the two-electron NOCI energy. This contraction scheme will be referred to as the unscaled algorithm.

The elements of the transition density matrix can be quite large due to the dependence on the inverse of the corresponding orbital overlap in eqn (6), which may prevent the direct algorithms from effectively screening unnecessary integrals. We propose to reformulate the two-electron part of the NOCI Hamiltonian by distributing the square-root of the determinant overlap $\mathbb{S}_{IJ}^{1/2}$ to the transition density matrix,

$$\sum_{\mu\nu} \mathbb{S}_{IJ} \mathbf{D}_{IJ,\mu\nu} \mathbf{G}_{IJ,\mu\nu}[\mathbf{D}_{JI,\lambda\kappa}] = \sum_{\mu\nu} \mathbb{S}_{IJ}^{1/2} \mathbf{D}_{IJ,\mu\nu} \mathbf{G}_{IJ,\mu\nu} \left[\mathbb{S}_{IJ}^{1/2} \mathbf{D}_{JI,\lambda\kappa} \right] \quad (10)$$

This simple modification can increase the effectiveness of the integrals screening. In this paper, we will refer to this as the density scaled algorithm and we will investigate the effect of this screening in Sections 3.2 and 3.3.

Eqn (10) includes the generalized Slater–Condon rules, which suggest that an element is zero if there are more than two orbital differences between the two determinants. These differences are readily seen in the singular values of the corresponding orbitals. If there are two or less singular values that are zero then the two electron operator is nonzero (assuming the element is not zero by some other mechanism such as symmetry). Likewise, if there are three or more zeroes, then we know that the element will be zero. Here, we define a continuous measure based on the generalized Slater–Condon rules to predict whether a determinant coupling is likely to be zero.

For cases with small but not nonzero singular values we can compute

$$\Theta_{IJ} = \frac{\prod_i s_{IJ,ii}}{s_{IJ,00}s_{IJ,11}} \quad (11)$$

where $s_{IJ,00}$ and $s_{IJ,11}$ are the two smallest singular values assuming they are ordered from the smallest to the largest. Θ describes the largest residual overlap in the two-electron integral contraction. Θ ranges from one to zero with one when the generalized Slater–Condon rules suggest the element is nonzero, and approaching zero when they suggest the element is zero. Therefore, when Θ goes to zero so does the NOCI two-electron coupling, and we can use eqn (11) to screen for the need to compute the two-electron integrals. Here, we found that screening elements with a Θ less than 10^{-5} provided good performance and accuracy compared to the unscaled method.

2.3 NOCI oscillator strength

The NOCI oscillator strength can be computed by treating the dipole moment integrals as a one-electron operator using the generalized Slater–Condon rules. Thus, the dipole vector in the NOCI determinant basis is

$$\mathbb{M}_{IJ} = \mathbb{S}_{IJ} \sum_{\mu\nu} \mathbf{D}_{IJ,\mu\nu} \langle \mu | \mathbf{r} | \nu \rangle \quad (12)$$

where the last term is the electric dipole integral in the atomic orbital basis. To compute the oscillator strength we transform the dipole vector into the NOCI state basis,

$$\mathcal{M}_{mn} = \mathbb{C}_m^\dagger \mathbb{M} \mathbb{C}_n \quad (13)$$

Then the oscillator strengths (Ω_I) can be computed using

$$\Omega_{mn} = \frac{2(\mathcal{E}_m - \mathcal{E}_n)}{3} |\mathcal{M}_{mn}|^2. \quad (14)$$

3 Results and discussion

The X2C-NOCI method introduced here is implemented in the development version of Chronus Quantum.^{81,82} All benchmark timings were performed on an Intel Xeon W 2.5 GHz CPU using the Clang compiler version 12.0.5. The calculations were performed in parallel using 28 threads using Chronus Quantum. Additionally, screening of the two-electron terms was performed using the Schwarz inequality.⁸⁰

L_{2,3}-edge X-ray absorption spectroscopy features excitations from 2p core electrons into the frontier orbitals. Due to spin-orbit coupling, the 2p orbitals are split into p^{3/2} and p^{1/2} manifolds. The L-edge spectra of three molecular systems were computed: (1) SF₆, (2) [FeCl₆]^{−3}, (3) SiCl₄. The geometries for SiCl₄ and [FeCl₆]^{−3} were taken from ref. 83. For SF₆, the geometry was optimized using M06-2X⁸⁴ with the aug-cc-pVDZ basis set.⁸⁵ Throughout this article, we compute vertical excitations from these geometries.

To determine the optimal number of states to include in our NOCI, we performed an iterative search by steadily increasing

the number of optimized determinants until the energy range of each spectra was satisfied. During this search, we include reference virtual orbitals in the set of target orbitals (see appendix) manifold by manifold to ensure that all spin microstates are well represented. We observed little benefit in including further determinants once the energy range was satisfied (see Section 3.3).

The spectra were computed by first convoluting the eigenvalues and oscillator strengths with a Lorentzian broadening function followed by a convolution with a Gaussian function. For SiCl_4 , the full width at half max (FWHM) for the Lorentzian function was 0.15 eV and the standard deviation of the Gaussian was also 0.15 eV. For $[\text{FeCl}_6]^{3-}$, the FWHM was 0.40 eV and the standard deviation was 0.20 eV. For SF_6 , the FWHM was 0.30 eV and the standard deviation was 0.30 eV.

While the scalar relativistic effects of SF_6 and SiCl_4 are not large, the spin-orbit coupling is significant enough to lead to splitting of the peaks (see ESI†). While this effect can be well captured using perturbative techniques, this presents a unique challenge for excited state determinant optimizations. In two-component methods, such as X2C, spin symmetry is no longer maintained, which makes the excited state manifold more dense. Additionally, in X2C-NOCI it is necessary to perform an adequate scan over all of the states in a manifold to ensure that X2C-NOCI space is spin-complete. Previously, we demonstrated that the gBLW optimization scheme can be used to scan over excited state manifolds in an efficient manner while maintaining all of the microstates for a given spin manifold. Here, we apply this same scheme to the computation of hundreds of individually optimized determinants.

3.1 SF_6 $L_{2,3}$ -edge

In this section, we test the effect that optimization of the orbitals has on the overall spectrum, specifically looking at SF_6 . For SF_6 , we excited the 2p electrons into the first 88 reference virtual orbitals and then optimized the determinants, resulting in a total of 529 nonorthogonal determinants in the X2C-NOCI calculations. The set of reference orbitals are the ground state molecular orbitals (see Appendix 2). All of the determinants were optimized with X2C-gBLW and the Sapporo double zeta basis set with diffuse functions.^{86–89}

Here, we tested four levels of constraint in X2C-gBLW optimizations of excited determinants for X2C-NOCI calculations. Using $2p \rightarrow t_{2g}, e_g$ excitations as an example, these constraints can be described as:

- Completely frozen – the core (the unexcited electrons *e.g.*, 1s, 2s, *etc.*) and excited orbitals (*e.g.*, t_{2g} , e_g) are frozen. This scheme does not need any gBLW optimizations and is equivalent to the conventional orthogonal CI method within an active space.
- Frozen excited – the excited electron is kept frozen to the target orbital (*e.g.*, one of the t_{2g} orbitals). In this scheme, only the core subspace is subject to the gBLW optimization by mixing with virtual orbitals.
- Inactive mixing – The excited electron is only allowed to mix with virtuals outside the ligand-field orbitals, *i.e.*, virtual



Fig. 1 A general scheme showing the approximations used in the optimization strategies employed on SF_6 . The diagrams do not exactly represent SF_6 because many more electrons and orbitals are required. Each section represents a determinant diagram where the colors are used to show in which subspace the basis function and electron reside. Here, blue represents the core electrons subspace, orange represents the excited electron subspace, purple represents being in both the core electron and excited electron subspaces, and gray represents being excluded entirely. Each line represents a reference orbital (*i.e.* the ground state molecular orbitals), and the arrows represent electron occupation at the start of the calculations.

orbitals higher in energy than t_{2g} and e_g manifolds are included in the excited subspace. In this scheme, both the core and excited subspaces are subject to the gBLW optimization.

- Energy cutoff – including all higher energy orbitals outside an energy cut-off of 0.1 Hartree in the excited subspace. The purpose of this scheme is to allow the excited electron to mix with all virtual orbitals that are not degenerate with the target orbital. For instance, if an e_g orbital is selected as the target orbital, all higher energy virtuals except those in the e_g manifold are included in the excited subspace. Note that including nearby virtuals could lead to a large orbital rotation away from the target orbital, undesired population inversion, and potential redundancy in the NOCI determinant basis. For SF_6 , we only observed significant rotations away from the target orbital for a small number of determinants.

Fig. 1 presents the approximation schemes based on orbital diagrams. Colors are used to represent the subspaces that each reference molecular orbital is a member of. The reference molecular orbitals are the ground state molecular orbitals, but it is possible to use any reasonable set of reference molecular orbitals.⁶⁸ The electron configuration in Fig. 1 resemble those of a core excited state where a low energy orbital is removed from the space that acts as the hole. Then this electron is

occupied in a higher energy target orbital (orange). This target orbital is allowed to mix with the higher energy orbitals (purple) to optimize the energy.

The computed spectra for SF_6 are presented in Fig. 2. All peaks are uniformly shifted by -8.55 eV, -2.75 eV, -2.45 eV and -2.40 eV for the completely frozen, frozen excited, inactive mixing, and energy cutoff constraints, respectively. This series suggests that as the optimization space is increased, the shift to experiment decreases, indicating the variational nature of this method. Additionally, relaxation of the core electrons has the largest effect on the absolute position of the spectra. The difference in shift between completely frozen and energy cutoff constraints suggests that the orbital optimization accounts for at least 6.15 eV of the correlation energy in this system. The singular values, which represent the orbital overlaps with the ground state, suggest that nearly all core orbitals are rotated to optimize the energy.

For the computed spectra, we observe the largest changes of the features going from the completely frozen to the frozen excited constraint. For instance, the shoulder on the low frequency side of the peak at 185 eV becomes more apparent. Additionally, the set of peaks between 193–202 eV decrease in energy by roughly 4 eV and the oscillator strengths increase. The spectral features at 195–196 eV display a significant increase in intensity going from the frozen excited to the inactive mixing and energy cutoff constraints, due to the optimization of the excited electron. Furthermore, there are a

set of weakly absorbing Rydberg peaks between 176 eV and 180 eV that are observed using constraints that feature orbital optimization but are not observed in the completely frozen scheme. Overall, these results suggest that the inactive mixing scheme is the most efficient for two reasons. First, the SCF is generally easier to converge using this constraint compared to the energy cutoff scheme. Second, the spectrum is largely indistinguishable from the energy cutoff scheme, which indicates that accuracy is largely unaffected.

In Fig. 2, we also compare the $\text{L}_{2,3}$ -edge spectrum computed using X2C-NOCI to both experiment⁹⁰ and the computed spectrum in ref. 91 that used response theory (complex polarization propagator^{92,93}) with density functional theory (CAM-B3LYP). This system features a small spin-orbit splitting of 1.2 eV according to experiment. NOCI agrees well with a value of 1.3 eV. Overall, the X2C-NOCI computed spectrum agrees fairly well with both experiment and response theory. Notable differences include the peak at 185 features a shoulder on the high energy side that is not observed in the other two. Additionally, X2C-NOCI underestimates the intensity of the shoulder on the low frequency side of the 185 eV peak. However, the absolute NOCI frequencies are more accurate than the response theory results, which needed to be shifted by 7.01 eV. Both X2C-NOCI and response theory observe a set of peaks between 186 and 194 eV that are not specifically observed in experiment. Mulliken population analysis combined with the singular values of the corresponding orbitals suggest these are single-electron transitions into high energy sulfur d-orbitals (≈ 70 orbitals above the occupied set). This spectral feature is present in all schemes for orbital optimization that we tested, which suggests it is not an artifact of orbital optimization. These same features are seen in the completely frozen approximation, but they are at higher energy due to the neglect of orbital optimization. The significance of these peaks is not clear.

3.2 SiCl_4 $\text{L}_{2,3}$ -edge

For SiCl_4 , the calculations were performed with a series of basis sets to test the scaling of the X2C-NOCI algorithm and the effect that the screening algorithm presented in Section 2.1. The Sapporo basis set family^{86–89} was used. For the algorithmic scaling tests, all six 2p electrons were excited into first 40 reference virtual orbitals, resulting in a total of 241 determinants. Subsequently, all excited determinants were optimized using the inactive mixing scheme. For calculations using the Sapporo-dzp basis with diffuse functions, we computed the additional excitations into the next 28 virtual orbitals (a total of 409 nonorthogonal determinants in X2C-NOCI).

The computed and experimental spectra are displayed in Fig. 3. The spectra were shifted by -3.85 eV, -3.40 eV, -2.00 eV, and -2.00 eV for the DZP, DZP-all, TZP and TZP-all bases, respectively. Overall, we see similar results between the basis sets for the low energy peaks around 104–107 eV. However for the higher energy peaks, the effects of basis set quickly become apparent. The basis sets that include diffuse functions feature small peaks in the range of 108–110 eV. These peaks represent Rydberg excitations.⁹¹ In Fig. 3A, the spectra using basis sets that

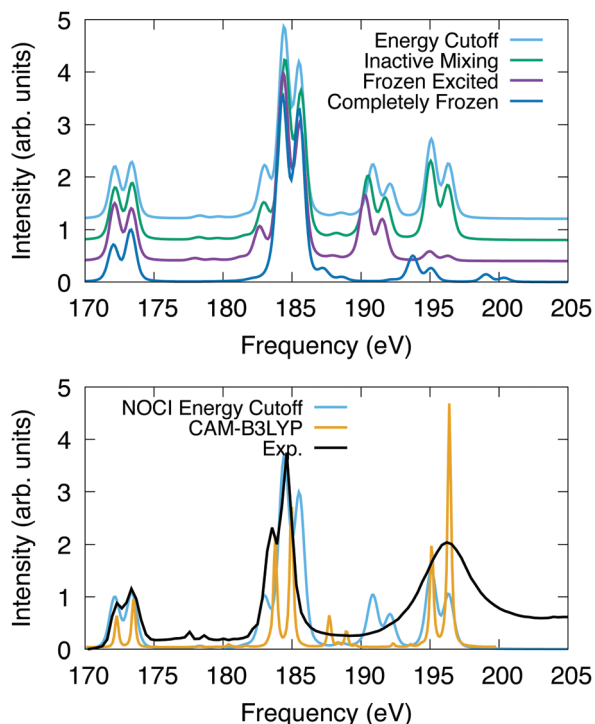


Fig. 2 $\text{L}_{2,3}$ edge X-ray absorption spectroscopy for SF_6 . The spectra were shifted and normalized to coincide with the peak at 173 eV. X2C-NOCI was performed using the Sapporo double zeta basis. The bottom plot also has the experimental spectrum,⁹⁰ and one computed using response theory with CAM-B3LYP.⁹¹

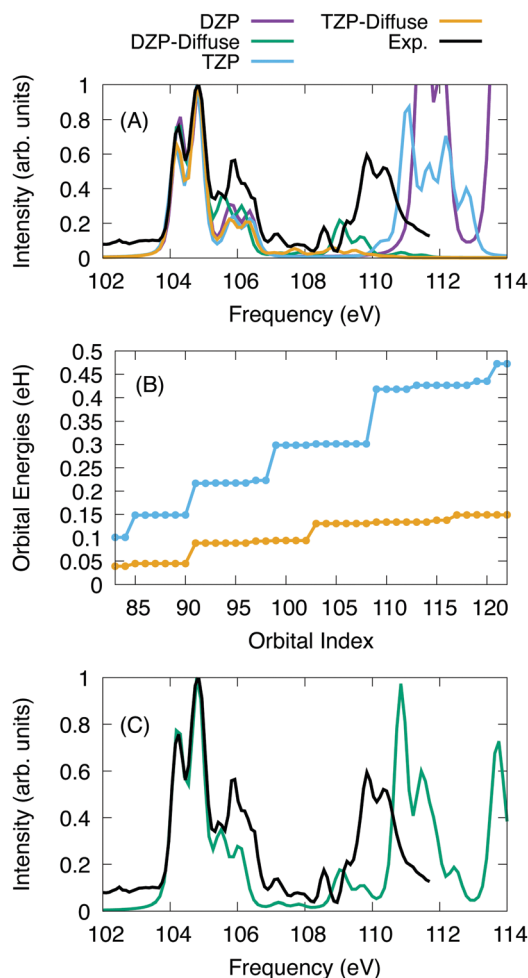


Fig. 3 (A) L_{2,3} edge X-ray absorption spectroscopy for SiCl₄ using only 241 determinants for all basis sets. The X2C-NOCI results were shifted and normalized to coincide with the tallest peak of the experimental spectrum. (B) X2C-HF Orbital energies of the reference target orbitals used in the gBLW optimization using the Sapporo triple zeta basis with and without diffuse functions. (C) L_{2,3}-edge experimental spectrum and NOCI computed with the Sapporo-DZP basis with diffuse functions with a larger X2C-NOCI space (409 determinants).

include diffuse functions go to zero at roughly 109 eV due to not including enough excitations to represent the higher energy features. Meanwhile for the basis sets without diffuse functions, none of the Rydberg peaks appear and the peaks around 110 eV are at higher energy by about 2 eV. Overall, the basis sets without diffuse functions are able to qualitatively describe the main features in the L_{2,3}-edge spectra of SiCl₄ but are missing the Rydberg states. The splitting of the two peaks between 104 and 105 eV is 0.59 eV, 0.60 eV, 0.63 eV and 0.63 eV for DZP, DZP-Diffuse, TZP and TZP-Diffuse, respectively. This compares well with the experimentally determined value of 0.61 eV. Additionally, for the full DZP-Diffuse spectrum (Fig. 3C) the strongly absorbing peak around 111 eV is higher than experiment by 1 eV.

To understand the origin of the large difference due to diffuse functions, the energies for the target excited orbitals are given in Fig. 3B. It is clear that including diffuse functions leads to a much slower increase in the orbital energy, which

means that the number of states needed to optimize for higher energies are greatly increased. Additionally, the excited state manifolds become more dense with many states providing little contribution to the final spectrum. For Sapporo-dzp with diffuse functions, we computed an additional 168 determinants (see Fig. 3C). This yields a better representation of the experimental peak at 109–110 eV, but it is higher in energy by about 1 eV. Overall, as one increases the size of the one-particle basis set, the NOCI becomes more accurate. However, the number of states required to represent the same energy range may increase also.

We tested the effective scaling of X2C-NOCI when using the AO direct algorithm (eqn (7)) with the improved integral screening using overlap-scaled density. Since the dominant computational cost in X2C-NOCI is the AO direct Fock build, the effective scaling can be computed using⁸⁰

$$\ln(t) \propto \alpha \ln(N_B) \quad (15)$$

where t is the CPU time and N_B the number of basis functions. α is the effective scaling. In Fig. 4, we have plotted the natural logarithms of the CPU time versus the number of basis functions. A determination of the slope can then be used to estimate the overall scaling of X2C-NOCI with respect to the number of basis functions. We yield a scaling of $N_B^{2.4}$, suggesting that the screening techniques in AO-direct algorithm can significantly lower the scaling of the X2C-NOCI approach. However, we did not observe a significant difference between the overlap scaled and unscaled algorithms for this system. Because we are only performing single excitations and there are not large rotations away from the reference orbitals, there is not a significant performance increase using the overlap scaled screening. We have included the timing information and number of basis functions in the ESI.†

3.3 [FeCl₆]^{3−} L_{2,3}-edge

For [FeCl₆]^{3−}, we excited the 2p electrons into first 43 reference virtual orbitals, resulting in a total of 259 nonorthogonal

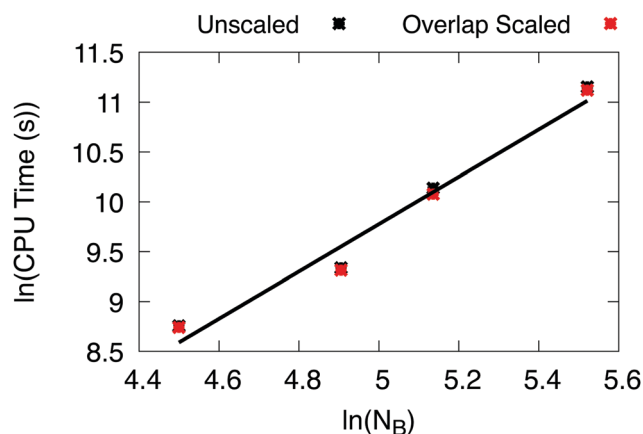


Fig. 4 Natural logarithms of the number of basis functions versus CPU time to compute the NOCI Hamiltonian using the improved screening algorithm. This data was fitted to a linear function to yield $\alpha = 2.4$.

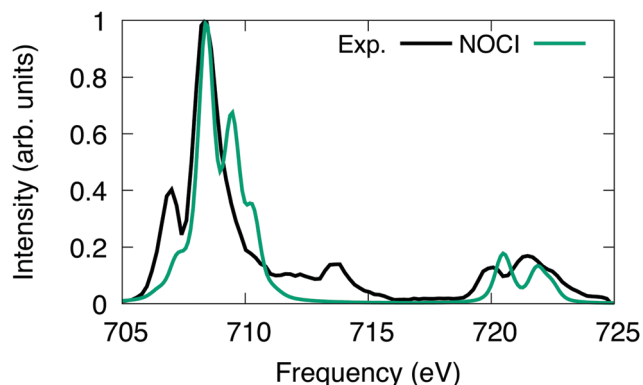


Fig. 5 $[\text{FeCl}_6]^{3-}$ L-edge spectrum computed using NOCI compared to experiment.¹⁰⁰ The computed NOCI spectrum has been shifted down by 9.9 eV to align with the first peak in the experiment.

determinants. The X2C-HF determinants were optimized using the Sapporo double zeta basis set with diffuse functions.^{86–89} The X2C-NOCI $L_{2,3}$ -edge spectrum has been shifted and renormalized to have the largest peak coincide with the experiment.

Overall, we observe good agreement between the X2C-NOCI computed spectrum and the experimental spectrum (Fig. 5). The experimental peaks at ~ 713 eV involve both single and double excitations in the form of shake-up peaks. There are several papers already in the literature that perform peak assignment for this system.^{94,95} Thus, our goal here is to evaluate the performance and accuracy of X2C-NOCI for computing L-edge spectra. Even though the X2C-NOCI method is capable of computing double excitations,⁶⁷ we will leave the optimization of doubly excited determinants to a future study. The X2C-NOCI spectrum displays shoulders on the higher energy side of L_2 edge. Orbital analysis suggests that these are transitions from the $p_{3/2}$ to orbitals dominated by the iron d-orbitals with some mixing with the chlorine s and d orbitals. The agreement on the higher energy L_3 peaks between 720 and 725 eV for both the relative energy and relative oscillator strength is excellent. However, for the L_2 edge, we observe a shoulder on the high frequency side of the largest peak which is not observed in experiment. Examining the largest contributions to these states suggest that these are single excitation states (*i.e.*, only one orbital difference in the singular values of the corresponding orbitals to the ground state). Furthermore, we computed an additional 156 optimized determinants and did not observe a significant change in the spectrum. The energies of the most significant peaks featured small changes on the order of 10^{-5} eV, and no additional features arise in the

extended calculation. It is possible that the intensity and positions of these peaks require higher order correlations and vibronic couplings. This effect warrants further development and investigation. The X2C-NOCI computed spectrum was shifted down by 9.9 eV. We suspect this large shift is due to lack of dynamic correlation. There are published methods for including dynamic correlation in NOCI through perturbation theory,^{96–99} configuration interaction,^{11,31} and density functional theory.^{17,21,23}

The $[\text{FeCl}_6]^{3-}$ molecule provides an interesting test for the screening of the two electron terms in the NOCI Hamiltonian. Here, there are a number of low lying reference orbitals that readily mix during the optimization of the excited states. Thus, there are many states where the corresponding orbitals between the excited and ground state determinants have multiple (more than two) singular values that are less than 0.1. Therefore, the screening techniques presented in Section 2.1 are more likely to be effective.

In Table 1, we display the speed-ups (ratios of CPU times) in forming the X2C-NOCI Hamiltonian using overlap-scaled density ($S_{IJ}^{1/2}D_{IJ}$ in eqn (10)), and overlap-scaled density with Slater–Condon estimation (eqn (11)), respectively, compared to using the unscaled density (D_{IJ} in eqn (9)). The density-contracted Cauchy–Schwarz integral screening scheme with a threshold of 10^{-12} is used. Overall, we observed significantly faster computation of the Hamiltonian using both the overlap-scaled density and also with Slater–Condon screening. With the latter we observe a speed-up of roughly 1.6 times compared to the conventional algorithm using unscaled density. To make sure we are not introducing too large of an approximation, we computed the error in the energy eigenvalues compared to the conventional algorithm. We observe a very small error with the maximum error being less than 10^{-4} eV and the mean unsigned error being less than 10^{-6} eV. Overall, the improved screening techniques show significant reduction in computational cost compared to the conventional algorithm when computing systems where there are large rotations among the core electrons.

To further examine the effects of the screening, we plotted the amount of time it takes to compute the two electron terms as a heat map with respect to the determinant index (Fig. 6). For the algorithm using unscaled density (Fig. 6A), we see that the amount of time it takes to compute the two-electron terms is roughly constant regardless of the nature of the two determinants. A histogram of the number of Hamiltonian elements with respect to time is given in the inset, and shows that the two electron coupling takes roughly 1.8 seconds to compute with little variance.

Table 1 Timing and error information for $[\text{FeCl}_6]^{3-}$ NOCI using the improved integral screening and the improved integral screening plus the Slater–Condon screening algorithms in comparison to the traditional algorithm

Algorithm	Speed up	MUE ^a (eV)	ME ^b (eV)
Unscaled density	1.0	—	—
Overlap-scaled density	1.4	2.0×10^{-7}	1.5×10^{-5}
Overlap-scaled density + Slater–Condon screening	1.6	2.0×10^{-7}	1.5×10^{-5}

^a Mean unsigned error of the energy eigenvalues. ^b Maximum error of the energy eigenvalues.

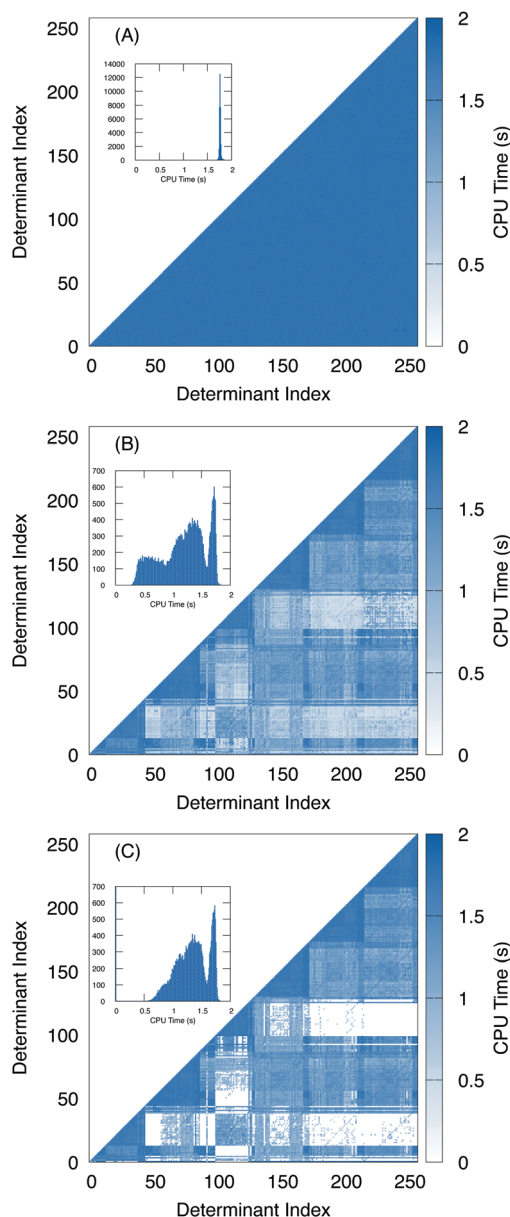


Fig. 6 Heat maps of the time to compute each of the two electron terms (CPU time) with respect to the determinant index using the unscaled density (A) vs. the overlap-scaled density algorithm (B) and the overlap-scaled density with the Slater–Condon screening (C). A histogram of each set of timings (summed over all respective elements) are included in the inset.

In contrast, with the overlap-scaled density (Fig. 6B) we observe a large variance in the timing ranging from less than half a second to roughly 1.8 seconds. Furthermore, in the heat map we see that most of the time-saved is in computing the off-diagonal elements. Here, the determinants are ordered by the origin of the excitation. Thus, the first group are all of the excitations from the lowest energy electron. Then all of the excitations from the next lowest electron. Since we are interested in the $L_{2,3}$ -edge X-ray spectrum, we are exciting the 2p electrons, which means there are six groups of excitations. This is observed in the heat map where the two

electron terms that take the longest time to compute are associated with determinants from the same group. Meanwhile, the blocks between excitation groups are the ones that exhibit the most screening. This is to be expected because the determinants have a difference of roughly two or more electrons depending on how much mixing the core electrons have with the frontier orbitals. Meanwhile, since the Slater–Condon screening is able to estimate that Hamiltonian terms are close to zero and can skip the computation entirely, addition speed-up is observed (Fig. 6C).

4 Conclusions

In this work, we introduced a variational relativistic non-orthogonal configuration interaction method using the exact-two-component transformation (X2C-NOCI). The generalized block localized wave function (gBLW) technique was used to optimize determinants of interest where relativistic effects (scalar relativity and spin-orbit) are variationally included for describing the X2C-NOCI wave function.

We used nonorthogonal configuration interaction to compute the $L_{2,3}$ -edge spectra for several molecular systems including SF_6 , SiCl_4 and $[\text{FeCl}_6]^{3-}$. Overall, X2C-NOCI is able to recover the main features of the $L_{2,3}$ -edge spectra.

We tested the effects that orbital relaxation has on the final spectrum using SF_6 . Overall, relaxation of the core electrons leads to the largest change in both the absolute energy and relative changes in the spectral features. Furthermore, we suggest that the inactive mixing approximation is the most efficient both in terms of SCF convergence and scanning the excited state manifold.

We proposed a screening technique using the overlap-scaled density matrix and a measure defined based on the generalized Slater–Condon rules for estimating which NOCI elements are zero before computing the two-electron term. This improved screening significantly increases the efficiency of the NOCI especially for a system where large rotations away from the reference orbitals are common such as in $[\text{FeCl}_6]^{3-}$. This lead to 1.6 times faster evaluation of the X2C-NOCI Hamiltonian compared to the conventional method. Meanwhile, these screening techniques introduced almost no error into the X2C-NOCI energy eigenvalues showing a mean unsigned error of 2.0×10^{-7} eV.

The X2C-NOCI method developed in this work has several unique advantages for the computation of X-ray spectroscopy. First, in the X2C-NOCI scheme, we are optimizing all of the determinants in the two-component framework so that each spin-orbit micro-state is at a variational minimum and all micro-states are treated on an equal-footing. Second, since spin-orbit couplings are included variationally at the orbital level, there is no need to use perturbative techniques.¹⁰¹ Although the tests carried out in this work can be readily done with perturbative techniques, it remains to be seen when variational X2C-NOCI is necessary when the subject matter contains heavier elements. A systematic benchmark is needed

and will be a future work. Third, the resulting CI reference wave function is more compact than the conventional orthogonal CI method for a given chemical problem (see ref. 102 for the size of CI space needed for $[\text{FeCl}_6]^{3-}$), making it an attractive method for multireference CI (MRCI) or second-order perturbation (MRPT) treatment of dynamic correlation. However, challenges abound. Constrained optimizations to generate nonorthogonal determinants may not converge when orbitals in different subspaces have significant overlap. The nonorthogonal MRCI and MRPT treatments are nontrivial because the external space in MRCI/MRPT can be redundant with respect to the NOCI orbital rotation. The authors envision that variational relativistic NOCI will become a unique tool for resolving certain challenging chemical problems (*e.g.*, L- and M-edge spectra). Of course, further developments and extensive benchmarks are needed to characterize this new variational relativistic NOCI framework.

Author contributions

A. G. performed the software implementation, data acquisition and data analysis. Both A. G. and X. L. contributed to conception/design of the study along with writing/revision of the article.

Conflicts of interest

There are no conflicts to declare.

Appendix A

A.1 Exact-two-component transformation

In this appendix, we briefly outline the exact-two-component transformation.

The restricted kinetically-balanced (RKB) Dirac equation in matrix representation is:^{103,104}

$$\begin{pmatrix} V & T \\ T & \frac{1}{4c^2}W - T \end{pmatrix} \begin{pmatrix} C_L^+ & C_L^- \\ C_S^+ & C_S^- \end{pmatrix} = \begin{pmatrix} S & 0_2 \\ 0_2 & \frac{1}{2c^2}T \end{pmatrix} \begin{pmatrix} C_L^+ & C_L^- \\ C_S^+ & C_S^- \end{pmatrix} \begin{pmatrix} \varepsilon^+ & 0_2 \\ 0_2 & \varepsilon^- \end{pmatrix}$$

$$W = (\vec{\sigma} \cdot \vec{p})V(\vec{\sigma} \cdot \vec{p}) \quad (16)$$

where the W term gives rise to relativistic corrections and spin couplings in an atomic/molecular system. c is the speed of light. V , T , and S are the two-component non-relativistic potential energy, kinetic energy, and overlap matrices, respectively. \vec{p} is the linear momentum operator and $\vec{\sigma}$ is the vector of Pauli matrices. The solutions of eqn (16) include sets of positive/negative eigenvalues ($\{\varepsilon^+\}$, $\{\varepsilon^-\}$) with corresponding molecular orbital coefficients $(C_L^+ C_S^+)^T$ and $(C_L^- C_S^-)^T$.¹⁰⁵

Usually, only the positive energy solutions, $\{\varepsilon^+\}$, are important for chemical systems.

The exact-two-component (X2C)^{47–66} method seeks to “fold” the small component coefficients into the large component by a one-step unitary transformation U ,

$$U \begin{bmatrix} \psi^L \\ \psi^S \end{bmatrix} = \begin{bmatrix} \tilde{\psi}^L \\ 0 \end{bmatrix} \quad (17)$$

resulting in an electron-only Hamiltonian. In X2C, the transformation matrix takes the form (see ref. 56 for numerical implementations)

$$U = \begin{pmatrix} 1_2 & -Y^\dagger \\ Y & 1_2 \end{pmatrix} \begin{pmatrix} (1_2 + Y^\dagger Y)^{-1/2} & 0_2 \\ 0_2 & (1_2 + Y Y^\dagger)^{-1/2} \end{pmatrix}, \quad (18)$$

$$Y = C_S^+ (C_L^+)^{-1} \quad (19)$$

In this work, we employ the one-electron X2C approach which is a one-step procedure to construct the transformation matrix through the diagonalization of the one-electron four-component core Hamiltonian. However, since the two-electron spin-orbit terms contribute with an opposite sign to the spin-orbit terms, we used the Boettger factors to scale the one-electron spin-orbit effect to semi-empirically treat the two-electron spin-orbit terms.⁷⁶

A.2 Generalized block localized wave function

Here, we only present a brief review on the X2C-gBLW method and how it can be used to compute nonorthogonal excited determinants.^{67,68}

We use the following notations to keep track of the nature of the index with respect to the basis.

- The Greek letters (μ , ν , λ , σ) index atomic spin orbitals (AO's)
- The primed Greek letters (μ' , ν' , λ' , σ') index transformed bases that span wave functions in a subspace
- The lowercase Latin letters (i , j , k) index occupied molecular orbitals (MO's)
- (A) indexes subspaces in generalized block-localized wave function (gBLW)

The gBLW method optimizes a set of molecular orbitals for a given determinant subject to constraints which are often based on chemical intuitions (*e.g.*, $\pi \rightarrow \pi^*$ transition). The constraints are encoded in a transformation from the original space of N basis functions to a set of subspaces. Molecular orbitals of each subspace ($\psi_{A,i}$) are linear combinations of transformed bases that are defined by the gBLW transformation matrix ($\psi_{A,\nu\nu'}$)

$$\psi_{A,i} = \sum_{j\nu'} C_{A,i\nu'} T_{A,\nu\nu'} \chi_{\nu'}, \quad \nu' \in A \quad (20)$$

C_A is the subspace coefficient matrix that is variationally optimized during the self-consistent field (SCF). T_A is a rectangular transformation matrix of dimension $N \times N_A$ where N is the total number of atomic basis functions and N_A is the number of selected transformed bases that span subspace A.

The SCF is performed by solving independent Roothaan–Hall equations for each subspace.

$$\mathbf{F}_A \mathbf{C}_A = \mathbf{S}_A \mathbf{C}_A \mathbf{e}_A \quad (21)$$

$$\mathbf{F}_A = \mathbf{T}_A^\dagger \mathbf{P}_A^\dagger \mathbf{F} \mathbf{P}_A \mathbf{T}_A \quad (22)$$

$$\mathbf{S}_A = \mathbf{T}_A^\dagger \mathbf{S} \mathbf{P}_A \mathbf{T}_A \quad (23)$$

Here, \mathbf{F}_A , \mathbf{S}_A , \mathbf{e}_A are the subspace Fock, overlap, and energy eigenvalue matrices, respectively. \mathbf{F} and \mathbf{S} are the full AO space Fock and overlap matrices, respectively. \mathbf{P}_A is the subspace projection matrix, which is defined as

$$\mathbf{P}_A = \mathbf{1} - \mathbf{D} \mathbf{S} + \mathbf{D}_A \mathbf{S} \quad (24)$$

where \mathbf{D} and \mathbf{D}_A are the density matrices for the full system and the subspace, respectively. $\mathbf{1}$ is the unit matrix. The density matrices can be computed using

$$D_{\mu\nu} = \sum_{ij} C_{\mu i} S_{ij}^{-1} C_{\nu j}^* \quad (25)$$

$$D_{A,\mu'\nu'} = \sum_{ij} C_{A,\mu' i} S_{A,ij}^{-1} C_{A,\nu' j}^* \quad (26)$$

where S_{ij} and $S_{A,ij}$ are the occupied molecular orbital overlap for the full space and the subspace, respectively. In general, the molecular orbitals are orthogonal within a subspace, but non-orthogonal between subspaces.

To compute an excited state determinant,⁶⁸ we first define a reference state from which to get a set of molecular orbitals that well represent the problem. Subsets of the reference molecular orbitals comprise the gBLW transformation matrix. Orbitals that are excluded from a subspace are absent in the transformation matrix, which eliminates their contribution to the subspace.

For a given gBLW determinant, we separate the electrons into two subspaces: (1) a subspace to represent the core electrons that remain in roughly the ground state configuration, (2) a subspace to represent the excited electron. Different constraints are employed on the two spaces to yield the best representation of the excited state. For the core electrons, the occupied orbitals of the reference state are usually allowed to mix with all orbitals except hole orbital from which the excited electron is excited, which prevents variational collapse. Additionally, we exclude the orbital we wish to occupy by the excited electron (the target orbital) to avoid redundancies that prevent convergence of the SCF procedure.

Meanwhile, the excited electron subspace includes the target orbital along with all virtual orbitals of the reference that are higher in energy. These higher energy orbitals mix with the target orbital to lower the energy of the determinant. Additional reference orbitals can be excluded from the excited electron space to aid in convergence of the self-consistent field, to guarantee that target states are represented in the determinant expansion, or to provide further understanding of the determinant optimization.⁶⁸ For nonorthogonal configuration interaction (NOCI), a set of determinants that span the excited manifold of interest are optimized. Thus, excluding orbitals from the excited electron space could be used to prevent large rotations away from the target orbital. While these rotations

away from the target orbital are useful for obtaining a variational minimum, it makes it more difficult to ensure the proper scanning of an excited state manifold. Thus, it may prevent the optimization of a spin-complete set of determinants. The effect of these constraints is tested in Section 3.1.

After all subspace MOs are fully optimized, all occupied orbitals from all subspaces are orthogonalized using Löwdin orthonormalization to yield a set of orthonormal molecular orbitals.

The procedure illustrated above is carried out for each desired gBLW determinant to be used in the NOCI calculation. Note that occupied MOs in each gBLW determinant are orthogonal but can be nonorthogonal to MOs that belong to a different gBLW configuration.

Acknowledgements

A. G. thanks Ruxin Qu for help in creating the figures. X. L. acknowledges support from the US Department of Energy, Office of Science, Basic Energy Sciences, in the Heavy-Element Chemistry program (Grant No. DE-SC0021100) for the development of relativistic electronic structure methods. The study of L-edge XAS is supported by the Ultrafast Initiative of the US Department of Energy, Office of Science, Office of Basic Energy Sciences, through Argonne National Laboratory under Contract No. DE-AC02-06CH11357.

Notes and references

- 1 P. O. Löwdin, *Phys. Rev.*, 1955, **97**, 1509–1520.
- 2 R. J. Harrison, *J. Chem. Phys.*, 1991, **94**, 5021–5031.
- 3 A. A. Holmes, N. M. Tubman and C. J. Umrigar, *J. Chem. Theory Comput.*, 2016, **12**, 3674–3680.
- 4 N. M. Tubman, C. D. Freeman, D. S. Levine, D. Hait, M. Head-Gordon and K. B. Whaley, *J. Chem. Theory Comput.*, 2020, **16**, 2139–2159.
- 5 J. B. Schriber and F. A. Evangelista, *J. Chem. Theory Comput.*, 2017, **13**, 5354–5366.
- 6 S. Shaik and P. C. Hiberty, *A Chemist's Guide to Valence Bond Theory*, John Wiley & Sons, Ltd, 2007.
- 7 W. Wu, P. Su, S. Shaik and P. C. Hiberty, *Chem. Rev.*, 2011, **111**, 7557–7593.
- 8 Z. Chen and W. Wu, *J. Chem. Phys.*, 2020, **153**, 090902.
- 9 P. C. Hiberty and S. Shaik, *Theor. Chem. Acc.*, 2002, **108**, 255–272.
- 10 D. L. Cooper and J. Gerratt, *Chem. Soc. Rev.*, 1997, **26**, 87–100.
- 11 S. Ten-no, *Theor. Chem. Acc.*, 1998, **98**, 182–191.
- 12 M. Head-Gordon, P. E. Maslen and C. A. White, *J. Chem. Phys.*, 1998, **108**, 616–625.
- 13 Q. Wu, C. L. Cheng and T. Van Voorhis, *J. Chem. Phys.*, 2007, **127**, 164119.
- 14 B. Kaduk, T. Kowalczyk and T. Van Voorhis, *Chem. Rev.*, 2012, **112**, 321–370.

- 15 A. J. W. Thom and M. Head-Gordon, *Phys. Rev. Lett.*, 2008, **101**, 193001.
- 16 A. J. Thom and M. Head-Gordon, *J. Chem. Phys.*, 2009, **131**, 124113.
- 17 A. Cembran, L. Song, Y. Mo and J. Gao, *J. Chem. Theory Comput.*, 2009, **5**, 2702–2716.
- 18 Y. Mo, P. Bao and J. Gao, *Phys. Chem. Chem. Phys.*, 2011, **13**, 6760–6775.
- 19 H. Ren, M. R. Provorse, P. Bao, Z. Qu and J. Gao, *J. Phys. Chem. Lett.*, 2016, **7**, 2286–2293.
- 20 J. Gao, A. Grofe, H. Ren and P. Bao, *J. Phys. Chem. Lett.*, 2016, **7**, 5143–5149.
- 21 A. Grofe, X. Chen, W. Liu and J. Gao, *J. Phys. Chem. Lett.*, 2017, **8**, 4838–4845.
- 22 L. Yang, A. Grofe, J. Reimers and J. Gao, *Chem. Phys. Lett.*, 2019, **736**, 136803.
- 23 R. Zhao, A. Grofe, Z. Wang, P. Bao, X. Chen, W. Liu and J. Gao, *J. Phys. Chem. Lett.*, 2021, 7409–7417.
- 24 Z. Chen, X. Chen and W. Wu, *J. Chem. Phys.*, 2013, **138**, 164119.
- 25 Z. Chen, X. Chen and W. Wu, *J. Chem. Phys.*, 2013, **138**, 164120.
- 26 Z. Chen, X. Chen, F. Ying, J. Gu, H. Zhang and W. Wu, *J. Chem. Phys.*, 2014, **141**, 134118.
- 27 X. Chen, Z. Chen and W. Wu, *J. Chem. Phys.*, 2014, **141**, 194113.
- 28 J. Olsen, *J. Chem. Phys.*, 2015, **143**, 114102.
- 29 S. Kähler and J. Olsen, *J. Chem. Phys.*, 2017, **147**, 174106.
- 30 S. Kähler and J. Olsen, *J. Chem. Phys.*, 2018, **149**, 144104.
- 31 T. Tsuchimochi and S. Ten-No, *J. Chem. Theory Comput.*, 2016, **12**, 1741–1759.
- 32 P. Å. Malmqvist, *Int. J. Quantum Chem.*, 1986, **30**, 479–494.
- 33 P. Å. Malmqvist and B. O. Roos, *Chem. Phys. Lett.*, 1989, **155**, 189–194.
- 34 P. Å. Malmqvist, B. O. Roos and B. Schimmelpfennig, *Chem. Phys. Lett.*, 2002, **357**, 230–240.
- 35 F. Lipparini and J. Gauss, *J. Chem. Theory Comput.*, 2016, **12**, 4284–4295.
- 36 H. J. A. Jensen, K. G. Dyall, T. Saue and K. Fægri, *J. Chem. Phys.*, 1996, **104**, 4083–4097.
- 37 J. Thyssen, T. Fleig and H. J. A. Jensen, *J. Chem. Phys.*, 2008, **129**, 034109.
- 38 A. Almoukhalalati, S. Knecht, H. J. A. Jensen, K. G. Dyall and T. Saue, *J. Chem. Phys.*, 2016, **145**, 074104.
- 39 S. Knecht, H. J. A. Jensen and T. Saue, *Nat. Chem.*, 2019, **11**, 40–44.
- 40 J. E. Bates and T. Shiozaki, *J. Chem. Phys.*, 2015, **142**, 044112.
- 41 R. D. Reynolds, T. Yanai and T. Shiozaki, *J. Chem. Phys.*, 2018, **149**, 014106.
- 42 T. Shiozaki and W. Mizukami, *J. Chem. Theory Comput.*, 2015, **11**, 4733–4739.
- 43 B. Vlaisavljevich and T. Shiozaki, *J. Chem. Theory Comput.*, 2016, **12**, 3781–3787.
- 44 S. Knecht, O. Legeza and M. Reiher, *J. Chem. Phys.*, 2014, **140**, 041101.
- 45 S. Battaglia, S. Keller and S. Knecht, *J. Chem. Theory Comput.*, 2018, **14**, 2353–2369.
- 46 A. J. Jenkins, H. Liu, J. M. Kasper, M. J. Frisch and X. Li, *J. Chem. Theory Comput.*, 2019, **15**, 2974–2982.
- 47 H. Hu, A. J. Jenkins, H. Liu, J. M. Kasper, M. J. Frisch and X. Li, *J. Chem. Theory Comput.*, 2020, **16**, 2975–2984.
- 48 W. Kutzlenigg and W. Liu, *J. Chem. Phys.*, 2005, **123**, 241102.
- 49 W. Liu and D. Peng, *J. Chem. Phys.*, 2006, **125**, 044102.
- 50 D. Peng, W. Liu, Y. Xiao and L. Cheng, *J. Chem. Phys.*, 2007, **127**, 104106.
- 51 M. Ilias and T. Saue, *J. Chem. Phys.*, 2007, **126**, 064102.
- 52 W. Liu and D. Peng, *J. Chem. Phys.*, 2009, **131**, 031104.
- 53 W. Liu, *Mol. Phys.*, 2010, **108**, 1679–1706.
- 54 T. Saue, *ChemPhysChem*, 2011, **12**, 3077–3094.
- 55 Z. Li, Y. Xiao and W. Liu, *J. Chem. Phys.*, 2012, **137**, 154114.
- 56 D. Peng, N. Middendorf, F. Weigend and M. Reiher, *J. Chem. Phys.*, 2013, **138**, 184105.
- 57 F. Egidi, J. J. Goings, M. J. Frisch and X. Li, *J. Chem. Theory Comput.*, 2016, **12**, 3711–3718.
- 58 J. J. Goings, J. M. Kasper, F. Egidi, S. Sun and X. Li, *J. Chem. Phys.*, 2016, **145**, 104107.
- 59 L. Konecny, M. Kadek, S. Komorovsky, O. L. Malkina, K. Ruud and M. Repisky, *J. Chem. Theory Comput.*, 2016, **12**, 5823–5833.
- 60 F. Egidi, S. Sun, J. J. Goings, G. Scalmani, M. J. Frisch and X. Li, *J. Chem. Theory Comput.*, 2017, **13**, 2591–2603.
- 61 A. Petrone, D. B. Williams-Young, S. Sun, T. F. Stetina and X. Li, *Eur. Phys. J. B*, 2018, **91**, 169.
- 62 W. Liu and Y. Xiao, *Chem. Soc. Rev.*, 2018, **47**, 4481–4509.
- 63 C. E. Hoyer, D. B. Williams-Young, C. Huang and X. Li, *J. Chem. Phys.*, 2019, **150**, 174114.
- 64 T. F. Stetina, J. M. Kasper and X. Li, *J. Chem. Phys.*, 2019, **150**, 234103.
- 65 T. Zhang, J. M. Kasper and X. Li, Chapter two – Localized relativistic two-component methods for ground and excited state calculations, in *Annual Reports in Computational Chemistry*, ed. D. A. Dixon, Elsevier, 2020, vol. 16, pp. 17–37.
- 66 C. E. Hoyer and X. Li, *J. Chem. Phys.*, 2020, **153**, 094113.
- 67 A. Grofe, R. Zhao, A. Wildman, T. F. Stetina, X. Li, P. Bao and J. Gao, *J. Chem. Theory Comput.*, 2021, **17**, 277–289.
- 68 A. Grofe, J. Gao and X. Li, *J. Chem. Phys.*, 2021, **155**, 014103.
- 69 J. M. Kasper, T. F. Stetina, A. J. Jenkins and X. Li, *Chem. Phys. Rev.*, 2020, **1**, 011304.
- 70 P. Norman and A. Dreuw, *Chem. Rev.*, 2018, **118**, 7208–7248.
- 71 P. O. Löwdin, *Phys. Rev.*, 1955, **97**, 1474–1489.
- 72 A. T. Amos and G. G. Hall, *Proc. R. Soc. Lond.*, 1961, **263**, 483–493.
- 73 H. F. King, R. E. Stanton, H. Kim, R. E. Wyatt and R. G. Parr, *J. Chem. Phys.*, 1967, **47**, 1936–1941.
- 74 L. Song, J. Song, Y. Mo and W. Wu, *J. Comput. Chem.*, 2009, **30**, 399–406.
- 75 A. Szabo and N. S. Ostlund, *Modern Quantum Chemistry: Introduction to Advanced Electronic Structure Theory*, Dover Publications Inc, Mineola, New York, 1996.
- 76 J. C. Boettger, *Phys. Rev. B: Condens. Matter Mater. Phys.*, 2000, **62**, 7809–7815.

- 77 R. K. Kathir, C. De Graaf, R. Broer and R. W. A. Havenith, *J. Chem. Theory Comput.*, 2020, **16**, 2941–2951.
- 78 T. P. Straatsma, R. Broer, S. Faraji, R. W. A. Havenith, L. E. A. Suarez, R. K. Kathir, M. Wibowo and C. De Graaf, *J. Chem. Phys.*, 2020, **152**, 064111.
- 79 M. Häser and R. Ahlrichs, *J. Comput. Chem.*, 1989, **10**, 104–111.
- 80 D. L. Strout and G. E. Scuseria, *J. Chem. Phys.*, 1995, **102**, 8448–8452.
- 81 X. Li, E. F. Valeev, D. Williams-Young, F. Ding, H. Liu, J. Goings, A. Petrone and P. Lestrange, Chronus Quantum, Beta Version, 2016, <https://www.chronusquantum.org>.
- 82 D. B. Williams-Young, A. Petrone, S. Sun, T. F. Stetina, P. Lestrange, C. E. Hoyer, D. R. Nascimento, L. Koulias, A. Wildman, J. Kasper, J. J. Goings, F. Ding, A. E. DePrince III, E. F. Valeev and X. Li, *Wiley Interdiscip. Rev.: Comput. Mol. Sci.*, 2020, **10**, e1436.
- 83 J. M. Kasper, P. J. Lestrange, T. F. Stetina and X. Li, *J. Chem. Theory Comput.*, 2018, **14**, 1998–2006.
- 84 Y. Zhao and D. G. Truhlar, *Theor. Chem. Acc.*, 2008, **120**, 215–241.
- 85 T. H. Dunning, *J. Chem. Phys.*, 1989, **90**, 1007–1023.
- 86 T. Koga, H. Tatewaki, H. Matsuyama and Y. Satoh, *Theor. Chem. Acc.*, 1999, **102**, 105–111.
- 87 M. Sekiya, T. Noro, T. Koga and H. Matsuyama, *J. Mol. Struct.*, 1998, **451**, 51–60.
- 88 T. Noro, M. Sekiya, T. Koga and H. Matsuyama, *Theor. Chem. Acc.*, 2000, **104**, 146–152.
- 89 H. Tatewaki, T. Koga and H. Takashima, *Theor. Chem. Acc.*, 1997, **96**, 243–247.
- 90 E. Hudson, D. A. Shirley, M. Domke, G. Remmers, A. Puschmann, T. Mandel, C. Xue and G. Kaindl, *Phys. Rev. A: At., Mol., Opt. Phys.*, 1993, **47**, 361–373.
- 91 T. Fransson, D. Burdakova and P. Norman, *Phys. Chem. Chem. Phys.*, 2016, **18**, 13591–13603.
- 92 P. Norman, D. M. Bishop, H. Jorgen, A. Jensen and J. Oddershede, *J. Chem. Phys.*, 2001, **115**, 10323–10334.
- 93 P. Norman, D. M. Bishop, H. J. A. Jensen and J. Oddershede, *J. Chem. Phys.*, 2005, **123**, 194103.
- 94 R. V. Pinjari, M. G. Delcey, M. Guo, M. Odelius and M. Lundberg, *J. Chem. Phys.*, 2014, **141**, 124116.
- 95 R. V. Pinjari, M. G. Delcey, M. Guo, M. Odelius and M. Lundberg, *J. Comput. Chem.*, 2016, **37**, 477–486.
- 96 H. G. A. Burton and A. J. W. Thom, *J. Chem. Theory Comput.*, 2020, **16**, 5586–5600.
- 97 S. R. Yost, T. Kowalczyk and T. Van Voorhis, *J. Chem. Phys.*, 2013, **139**, 174104.
- 98 S. R. Yost and M. Head-Gordon, *J. Chem. Phys.*, 2016, **145**, 054105.
- 99 S. R. Yost and M. Head-Gordon, *J. Chem. Theory Comput.*, 2018, **14**, 4791–4805.
- 100 E. C. Wasinger, F. M. F. de Groot, B. Hedman, K. O. Hodgson and E. I. Solomon, *J. Am. Chem. Soc.*, 2003, **125**, 12894–12906.
- 101 M. L. Vidal, P. Pokhilko, A. I. Krylov and S. Coriani, *J. Phys. Chem. Lett.*, 2020, **11**, 8314–8321.
- 102 A. J. Jenkins, H. Hu, L. Lu, M. J. Frisch and X. Li, *J. Chem. Theory Comput.*, 2022, **18**, 141–150.
- 103 K. G. Dyall and K. Fægri, Jr., *Introduction to Relativistic Quantum Chemistry*, Oxford University Press, 2007.
- 104 M. Reiher and A. Wolf, *Relativistic Quantum Chemistry*, Wiley-VCH, 2nd edn, 2015.
- 105 S. Sun, T. F. Stetina, T. Zhang, H. Hu, E. F. Valeev, Q. Sun and X. Li, *J. Chem. Theory Comput.*, 2021, **17**, 3388–3402.